THE JOURNAL OF PHYSICAL CHEMISTRY C

Article

pubs.acs.org/JPCC

Quantitative Analysis of Trap-State-Mediated Exciton Transport in Perovskite-Shelled PbS Quantum Dot Thin Films Using Photocarrier Diffusion-Wave Nondestructive Evaluation and Imaging

Lilei Hu,[†] Zhenyu Yang,[‡] Andreas Mandelis,*[,†,‡] Alexander Melnikov,[†] Xinzheng Lan,[‡] Grant Walters,[‡] Sjoerd Hoogland,[‡] and Edward H. Sargent[‡]

[†]Center for Advanced Diffusion-Wave and Photoacoustic Technologies (CADIPT), Department of Mechanical and Industrial Engineering, University of Toronto, Toronto, Ontario M5S 3G8, Canada

[‡]Edward S. Rogers Sr. Department of Electrical and Computer Engineering, University of Toronto, Toronto, Ontario M5S 3G4, Canada

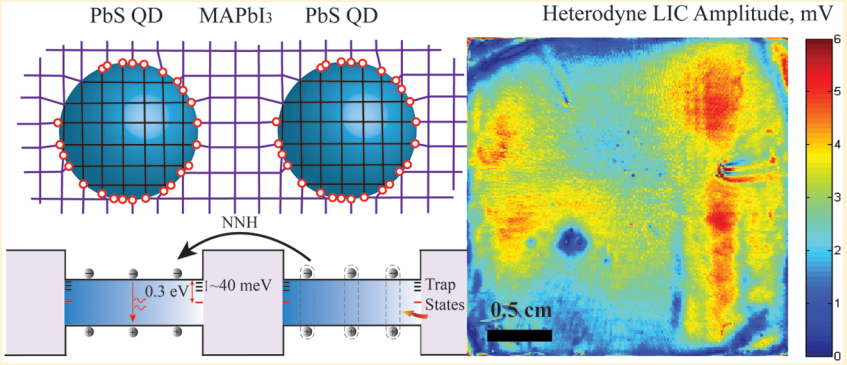

ABSTRACT: Perovskite-shelled colloidal quantum dots (CQDs) with low trap-state density are promising candidates for large-scale, low-cost, and lightweight solar cell applications. However, even minimal trap states can significantly limit CQD-based solar cell efficiency. We reported trap-state-mediated exciton transports in methylammonium lead triiodide ($MAPbI_3$) perovskite-passivated PbS CQD thin films. Excitation power-dependent photocarrier radiometry (PCR) intensity study demonstrated the free (electrons/holes)-to-bound (acceptors/donors) and trap-state-related transition-induced nonlinear response of CQD thin films to excitation. The existence of shallow trap states (activation energy: 33.8−40.7 meV) was characterized using photothermal emission spectra at different modulation frequencies. CQD thin films were imaged, for the first time, by InGaAs-camera-based nondestructive homodyne and heterodyne lock-in carrierographies (LIC; spectrally gated dynamic photoluminescence imaging), clearly showcasing photocarrier density diffusion-wave inhomogeneities that stem from defect-associated multiple effective exciton lifetimes. PCR frequency scans, coupled with the trap-state-mediated exciton transport model, extracted multiple material and carrier transport parameters such as effective exciton lifetime τ_E, hopping diffusivity D_h, dark and bright state separation energy ΔE, and carrier trapping rate N_T. Camera-based contactless homodyne and heterodyne LIC imaging of QD thin films was found to be a promising nondestructive characterization technique for monitoring optoelectronic qualities of QD materials and devices.

1. INTRODUCTION

Colloidal quantum dots (CQDs) are of great interest for potential applications in photovoltaic devices in view of their size-tunable bandgap, facile synthesis, high monodispersity, and solution process ability.[1−10] Recent progress in quantum dot surface chemistry and device architecture engineering has raised certified AM 1.5 solar power conversion efficiencies of CQD solar cells from 8% to 11.3%.[11−15] CQDs are soluble in variable solvents[16−23] which are suitable for multiple thin-film deposition processes ranging from layer-by-layer (LBL) spin coating,[24−26] to inkjet printing,[27,28] dip coating,[29−31] and spray coating.[32,33]

The thorough understanding of transport behaviors of charge carriers including excitons and free electrons and holes is essential for solar cell efficiency improvement; however, surface defects act as limiting factors for device optimization.[11,34] Therefore, studies of charge carrier recombination mechanisms to elucidate energy losses in CQD solid-state films are of great significance to CQD-based solar cells. Many efforts have been made toward this goal; for instance, Sun et al.[35] succeeded in reducing charge carrier recombination in PbS CQD solar cells through incorporating Zn-doped $CuInS_2$ QDs, which enhanced the charge separation probability between two types of QDs. Bozyigit et al.[36] used temperature-dependent current−voltage

Received: May 3, 2016
Revised: June 20, 2016
Published: June 22, 2016

DOI: 10.1021/acs.jpcc.6b04468
J. Phys. Chem. C 2016, 120, 14416−14427

characterization and thermal admittance spectroscopy to study PbS nanocrystal-based diodes and developed a systematic model for charge carrier transport, trapping, and recombination in different nanocrystals. They discovered that charge carrier transport in QDs was governed by a diffusion-controlled trap-assisted recombination process. Colbert et al.[37] observed charge carrier generation and recombination effects in hybrid polymer/QD solar cells through QD surface chemistry control.

However, for CQD solar cells, apart from energy loss to various charge carrier recombination processes, device imperfections induced in their fabrication process are also responsible for dissipating energy and undermining CQD solar cell efficiency. Therefore, all-optical, contactless, and non-destructive diagnostic techniques are in demand, especially for CQD substrates and devices due to their fragile material nature. Many techniques have been developed for the characterization of photovoltaic materials and devices. Electrical analysis including current−voltage and capacitance−voltage tests is the most direct and reliable method but is not applicable to unfinished solar devices or raw substrates. Direct-current (DC) photoluminescence (PL) imaging associated with Si charge-coupled devices (CCD) and InGaAs cameras can detect problems related to mechanical handling and imperfections (cracks) of raw substrates and solar devices, but it lacks the ability to monitor the kinetics of electronic transport and recombination properties which are responsible for the photovoltaic energy conversion and energy dissipation. Moreover, PL is unable to detect the optoelectronic kinetics of the surface and near-surface (junction) regions, which, however, are of key interest for solar cell efficiency enhancement.[38] Electroluminescence imaging of solar cells uses a camera that converts electric fields applied to the device to infrared radiative emission; however, this technique can only be applied to finished and operating solar cells and, thus, is not suitable for substrates and partly processed devices.[39] Homodyne and heterodyne carrierographies introduced by Mandelis et al.[40,41] as spectrally gated forms of dynamic PL are all-optical and contactless imaging techniques, which can monitor the kinetics of charge carrier transport in junction regions. These techniques are capable to map photogenerated charge carrier densities and lifetimes of Si-based photovoltaic substrates and devices.[42−46] In this paper, we studied charge carrier recombination processes and sub-bandgap energy states in perovskite passivated CQD thin films for photovoltaic applications using PL spectroscopy, excitation power-dependent PL intensity, and photocarrier radiometry (PCR)-based photothermal spectroscopy. We further applied homodyne and heterodyne lock-in carrierographies for the characterization of charge carrier diffusion-wave density distribution in CQD thin films. Quantitative analysis of carrier transport properties was carried out through PCR frequency scans and computational best-fits of an exciton hopping based PCR theoretical transport model to the data.

2. EXPERIMENTAL METHODS

Figure 1 is the schematic of the LIC imaging setup. Two 8 W fiber-coupled diode lasers of 808 nm wavelength were used for optical illumination. To obtain homogeneous illumination, both laser beams were spread and homogenized using diffusers to generate a 10 × 10 cm^2 square illumination area with small intensity variations (<5%). The employed high-speed NIR InGaAs camera (Goodrich SU320 KTSW-1.7RT/RS170) has the following features: 320 × 256 pixel active elements, spectral

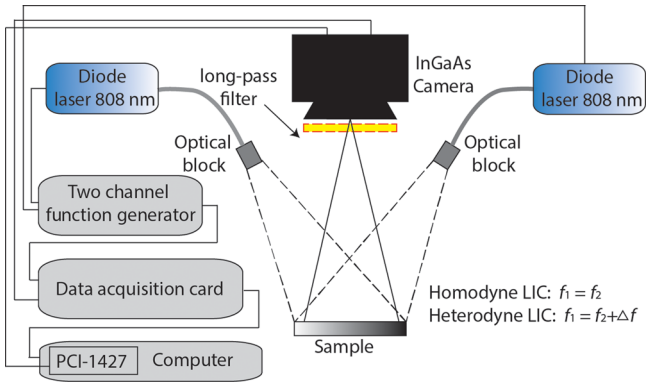

Figure 1. Experimental setup for homodyne and heterodyne lock-in carrierographic imaging.

bandwidth of 0.9−1.7 μm, 120 fps frame rate, and exposure times between 0.13 and 16.6 ms. Furthermore, the excitation laser beams were filtered through a long-pass filter (Spectrogon LP-1000 nm) placed in front of the InGaAs camera to avoid their influence on sample images. Due to the limitations of the camera frame rate, a synchronous undersampling method was employed through the application of a data acquisition module (NI USB-6259), which produced a reference signal and an external trigger to the camera. Sixteen images per period were scanned with a frame grabber (NI PCI-1427). Heterodyne carrierographic imaging was carried out by modulating two excitation laser frequencies of 20.00 and 20.01 kHz through a two-channel function generator. Amplitude images were extracted from in-phase (IP) and quadrature (Q) images at the beat frequency Δf = 10 Hz in the same manner as the homodyne LIC imaging. In addition, a 10 Hz reference signal and a trigger were created from the data acquisition module USB 6259. All measurements were performed in air atmosphere at room temperature in the dark.

To characterize charge carrier recombination processes and sub-bandgap states within CQD thin films, excitation laser intensity scans, PCR temperature (photothermal spectroscopy) scans, and laser modulation frequency scans were carried out with a conventional PCR system[47] using a single InGaAs detector (Thorlabs PDA400). For the excitation laser intensity scan, a density-variable rotational neutral density filter (Thorlabs NDC-100C-2M) was used. One percent of the emitted laser beam was split off for laser intensity monitoring. Two lock-in amplifiers were used to measure the PCR signal and laser intensity. Similarly, the excitation laser beam was filtered with a long-pass filter; hence, thermal-infrared waves were eliminated by the long-wavelength cutoff nature of the InGaAs detector. Temperatures were controlled by a Linkam LTS350 cryogenic stage that allowed maintaining constant temperatures in a range between 77 and 520 K for PCR temperature scans. The setup for PCR frequency scans was the same as that reported earlier.[48]

The CQD thin films studied in this work are of the lead sulfide (PbS) kind and were surface passivated with methylammonium lead triiodide perovskite ($MAPbI_3$) to remove CQD surface defect states and adjust interdot distances. The detailed fabrication process, as well as scanning electron microscopy (SEM) and transmission electron microscopy (TEM) images of these perovskite ($MAPbI_3$)-passivated CQD thin films, can be found in our previous report.[34] With excellent surface passivation of perovskite thin

DOI: 10.1021/acs.jpcc.6b04468
J. Phys. Chem. C 2016, 120, 14416−14427

shells onto CQD surfaces, the CQD solar cells exhibited improved open-circuit voltage and power conversion efficiency compared with those without $MAPbI_3$ treatment or those treated with other ligands.[34] Two CQD thin films (samples A and B) were fabricated with different free-exciton PL emission peaks for LIC imaging analysis toward qualitative thin-film homogeneity and mechanical defect characterization for the purpose of CQD solar cell efficiency optimization in our lab fabrication processes.

3. THEORETICAL METHODS

3.1. Charge Carrier Recombination Mechanism for PbS CQDs. To a great extent, semiconductor quality is determined by structural defects arising from dangling bonds on QD surfaces, such as point defects including vacancies and interstitials performing as very efficient trap states for electrons, holes, and excitons. They exhibit a strong influence on optical and electrical properties of the host semiconductor materials. In PbS QDs, potential point defects include Pb-vacancies (V_{Pb}), S-vacancies (V_s), Pb-interstitials (Pb_i), S-interstitials (S_i), and antisites (Pb_S and S_{Pb}). These possible defects can be introduced during the material fabrication process, acting as recombination centers. $MAPbI_3$ has been reported to be an excellent candidate for passivating PbS CQD surface defects because of the minimal lattice mismatch between the $MAPbI_3$ and PbS, a schematic shown in Figure 2(a). As a result, no defect-related peaks were found in PL spectra of $MAPbI_3$–PbS CQDs in solution.[34]

However, a better understanding of charge carrier recombination processes in CQD thin films is necessary. As shown in Figure 3, photogenerated excitons, free electrons, and holes may undergo the following transitions in PbS CQDs: radiative free-exciton recombination (FE), radiative acceptor- and donor-bound exciton (AX, DX) recombination, nonradiative donor–acceptor pair (DA) recombination, radiative recombination of a free electron and a neutral acceptor (eA), and radiative recombination of a free hole and a neutral donor (hD). These recombination processes have also been encountered in other low-dimensional nanosystems including ZnO nanocrystals,[49] MoS_2, $MoSe_2$, and WSe_2 monolayers,[50] ZnSe nanowires,[51] InGaN/GaN multiple quantum wells,[52] InAs/GaAsSb quantum dots,[53] and PbS quantum dots.[54] Unlike semiconductor materials with continuous energy bands, CQDs exhibit excitonic behaviors with photogenerated excitons having much higher binding energy than that of excitons in semiconductor materials with continuous energy bands and are incapable of forming continuous band structures due to the dot size polydispersity and the energy band disorder. Therefore, excitons are bound together and are not able to separate into free electrons and holes without the help of external forces including interdot coupling effects and electric fields.[55] Physical descriptions of processes (I) to (VI) in Figure 3 have been detailed by Schmidt et al.,[56] while for $MAPbI_3$–PbS CQDs, four unique conditions are considered: first, their n-type conducting property (only for calculation simplification), which, although not measured in this study, hinges on previous evidence of the n-type conducting property of CQD-perovskite LEDs;[2] second, exciton recombination dominates the transitions; third, excitons bound to ionized donors and acceptors can be neglected due to their weak transition probabilities; and fourth, the excitation laser energy is higher than the CQD bandgap E_g. Therefore, the rate formulas adapted from Schmidt et al.[58] can be expressed by

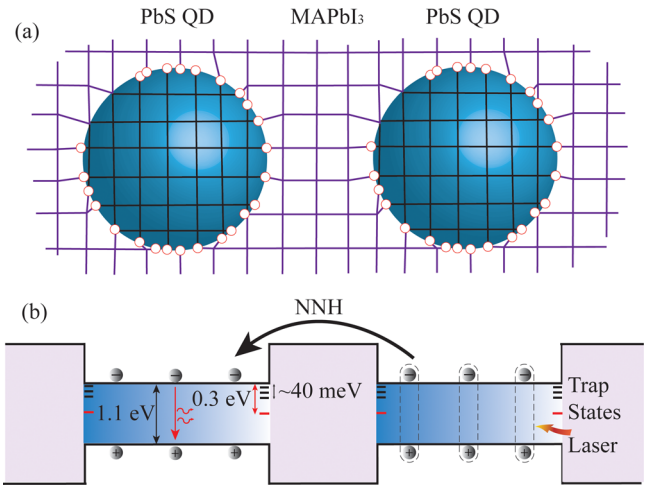

Figure 2. (a) Schematic of PbS QDs in $MAPbI_3$ matrixes, i.e., $MAPbI_3$-passivated PbS QDs. Due to the slight lattice mismatch, chemical bonds can be satisfied at the interfaces between QD and $MAPbI_3$, and the unsatisfied bonds act as surface trap states, denoted by red circles (a); (b) energy band structure (assumed n-type) of a PbS-$MAPbI_3$ nanolayer, sample A, featuring shallow and deep level trap states. Excitons are excited in the right QD and diffuse through nearest-neighbor hopping (NNH) to the next QD, during which process the coupling strength between two QDs dissociates excitons into free charge carriers. Carriers may experience radiative recombination or be captured by different types of trap states, where nonradiative recombination or detrapping may occur.

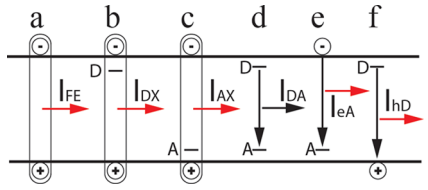

Figure 3. Near-band-edge photoluminescence via variable radiative and nonradiative transitions. (a) Free-exciton recombination, (b) and (c) recombination of donor (D)- and acceptor (A)-bound excitons (DX, AX), (d) donor–acceptor pair recombination (DA), (e) recombination of a free electron with a neutral acceptor (eA), and (f) recombination of a free hole with a neutral donor (hD).

$$\frac{dn}{dt} = gP - an^2 \tag{1}$$

$$\frac{dn_{FE}}{dt} = an^2 + P - \left(\frac{1}{\tau_{FE}} + \frac{1}{\tau_{FE}^{nr}}\right)n_{FE} - bn_{FE}N_{D^0} \tag{2}$$

$$\frac{dn_{DX}}{dt} = bn_{FE}N_{D^0} - \left(\frac{1}{\tau_{DX}} + \frac{1}{\tau_{DX}^{nr}}\right)n_{DX} \tag{3}$$

$$\frac{dN_{D^0}}{dt} = g(N_D - N_{D^0})n - mN_{D^0}P - bn_{FE}N_{D^0} + \left(\frac{1}{\tau_{DX}} + \frac{1}{\tau_{DX}^{nr}}\right)n_{DX} - fN_{D^0}n \tag{4}$$

where P is the excitation laser intensity; τ_{FE} and τ_{FE}^{nr} are the radiative and nonradiative lifetimes of free excitons, respectively; and τ_{DX} and τ_{DX}^{nr} are the respective radiative and nonradiative lifetimes of donor-bound excitons undergoing

DOI: 10.1021/acs.jpcc.6b04468
J. Phys. Chem. C 2016, 120, 14416–14427

transition DX. n, n_{FE}, and n_{DX} are the concentrations of free electrons, free excitons, and donor bound excitons, respectively. Furthermore, N_D and N_{D^0} are the concentrations of donors and neutral donors, respectively. a, b, ..., f are the coefficients associated with the processes shown in Figure 3, while g and m are coefficients for exciton generation and electron excitation, respectively. Solving eqs 2 and 3 in the steady state yields the luminescence intensities of free and bound excitons, I_{FE} and I_{DX}, defined as

$$I_{FE} \propto \frac{n_{FE}}{\tau_{FE}} = \frac{B}{\tau_{FE}} n^2 \tag{5}$$

$$I_{DX} \propto \frac{bN_D B}{1 + \frac{\tau_{DX}}{\tau_{DX}^{nr}}} n^2 \tag{6}$$

where

$$B = \frac{a}{\left(\frac{1}{\tau_{FE}} + \frac{1}{\tau_{FE}^{nr}}\right) + bN_D} \tag{7}$$

Provided the probabilities of free-to-bound transitions are proportional to the respective transition rates, luminescence intensities of free-to-bound (donors) transitions, I_{hD}, can be expressed by

$$I_{hD} \propto nN_{D^0} \tag{8}$$

Solving eq 1 in the steady state yields $n \propto P^{0.5}$. Using this relationship in eqs 5 to 8, it is found that $I \propto P$ for excitonic transitions and $I \propto P^{0.5}$ for free-to-bound transitions. Therefore, the γ value can be used to characterize the type of a radiative charge carrier recombination process. Experimentally, γ is generally measured to be between 1 and 2 for excitonic emissions including transitions (a)−(c) in Figure 3 and less than 1 for free-to-bound (acceptors/donors) emissions as shown by transitions (d)−(f). For example, $\gamma = 0.69$ for sub-bandgap recombinations and $\gamma = 1.48$ for band-edge associated recombinations for PbS-TBAI QD/PbS-EDT QD devices,[54] in which TBAI and EDT denote tetrabutylammonium iodide and 1,2-ethanedithiol, respectively. Therefore, the value of γ can be used to physically interpret the linear or nonlinear behavior of a charge carrier recombination process with respect to the laser excitation and reveals the underlying radiative recombination process. It is an important parameter for the LIC process because nonlinear PL responses to the laser excitation, acting as a nonlinear frequency mixer, are essential for PL-based heterodyne LIC imaging.[40,42,43,46]

As opposed to CQD thin films, excitons in polycrystalline and amorphous Si wafers, upon their formation, immediately dissociate into free electrons and holes, with the dominant recombination process being via defect states. In this situation, the nonlinear recombination term an^2 in the rate equation $\frac{dn}{dt} = gP - an^2 - hn(N_D - N_{D^0}) - enN_{A^0}$ (h is the coefficient for nonradiative transitions of free electrons to ionized donors, and N_{A^0} is the concentration of natural acceptors)[56] can be neglected, resulting in $n \propto P$. Solving eqs 5−8 using the relationship $n \propto P$, it follows that $I \propto P^2$ for excitonic transitions and $I \propto P$ for free-to-bound transitions. This conclusion is consistent with experimental LIC results for Si wafers with exponent $\gamma > 1$.[43]

3.2. Lock-In Carrierography Imaging. As depicted in Figure 3, when PbS CQD thin films are excited optically, excitons, electrons, and holes undergo radiative and non-radiative transitions. Surface-defect-induced trap states act as thermal emission and capture centers. The effects of such trap states have also been reported in thiol-capped PbS QDs,[58] glass-encapsulated PbS QDs,[59] and trap-related emission bands for PbS QDs in poly(vinyl alcohol).[60] The PCR signal is an integral of the charge carrier population over the thickness of the active layer:[47] $S(\omega) = F\int_0^d n(x,\omega)dx$, in which $S(\omega)$ is the linearized PCR signal as a function of the excitation laser beam modulation angular frequency ω; F is an instrumental coefficient that depends on the spectral detection emission bandwidth $[\lambda_1,\lambda_2]$ of the near-infrared detector; $n(x,\omega)$ is the depth-dependent charge carrier population; and d is the film thickness. The PCR signal from CQD thin films can be expressed as a function of the photogenerated carrier transport and recombination parameters[57]

$$\frac{S(\omega)}{F(\lambda_1, \lambda_2)} = \left[\frac{K_2(T,\beta)}{\beta^2 - K_1^2(T,\omega)}\right] \left\{\frac{(1 + e^{-\beta d})(1 - e^{-K_1(T,\omega)d})^2}{K_1(T,\omega)(1 - e^{-2K_1(T,\omega)d})} - \frac{1}{\beta}(1 - e^{-\beta d})\right\} \tag{9}$$

where the hopping diffusion wavenumber

$$K_1^2(T;\omega) \equiv \frac{1}{D_h(T)}\left\{i\omega + \frac{1}{\tau_E(T)} - \frac{N_T}{[1 + A(T)][1 + i\omega\tau_i(T)]}\right\} \tag{10}$$

and

$$K_2(T,\beta) \equiv \frac{G_0\beta}{D_h(T)[1 + A(T)]} \tag{11}$$

In these equations, T is the absolute temperature; $D_h(T)$ is the hopping diffusivity; β is the absorption coefficient of the excitonic medium; $\tau_E(T)$ is the temperature-dependent effective exciton lifetime; $\tau_i(T)$ is the corresponding detrapping lifetime; N_T is the trap state density determined carrier trapping rate; G_0 is the exciton generation rate; and $A(T)$ is defined as $A(T) = R_{st}e^{-\Delta E/kT}$, where ΔE is the energy difference between the split triplet−singlet excitonic energy levels, k the Boltzmann constant, and R_{st} an energy degeneracy constant equal to 1/3.

For homodyne LIC imaging, in order to overcome the camera frame rate limitation at high frequencies, a schematic of the LIC undersampling method is shown in Figure 4(a). With undersampling, one or more cycles are skipped between each image; for example, four images are taken at 0, $\pi/2$, π, and $3\pi/2$ phases (Figure 4(a)). The main pulse train plays the role of triggering the camera to start taking images, and the camera pulse train initiates four images to be taken during a fixed camera exposure period. By skipping more cycles, higher modulation frequencies can be used while keeping the camera frame rate unchanged.

With the application of the undersampling method, however, problems still arise when high modulation frequencies are used. They include the multiplicative nature of small timing errors and the decreased resolution due to the limited camera exposure time.[42,45] Therefore, a heterodyne method was introduced for high frequency LIC imaging through the

DOI: 10.1021/acs.jpcc.6b04468
J. Phys. Chem. C 2016, 120, 14416−14427

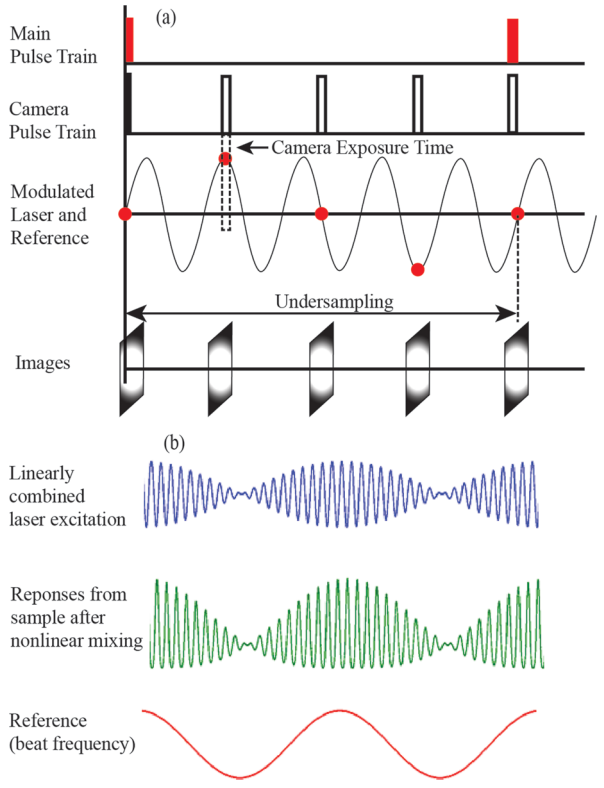

Figure 4. Schematics of camera-based LIC using an undersampling method (a) and modulation laser frequency mixing mechanism for heterodyne lock-in carrierography (b).

superposition of two modulated laser beams with a small frequency difference (the beat frequency) and the camera measuring with a frame rate equal to the beat frequency.[40] Figure 4(b) displays the image generation mechanism of heterodyne LIC imaging: two linearly combined laser irradiation modulation frequencies with a beat frequency of 10 Hz are mixed. The interaction between the two modulated excitation lasers and the sample is a nonlinear process that enables the generation of an LIC image at the beat frequency as shown in Figure 4(b). The camera reference modulation frequency is always selected to be equal to the beat frequency, i.e., 10 Hz in this study. The recorded image amplitudes carry information from the high modulation frequency. Phase images cannot be obtained at the beat frequency due to the close proximity of the two mixed frequencies f_1 and f_2 (Figure 1).

4. RESULTS AND DISCUSSION

Figure 5(a) shows PL spectra of perovskite $MAPbI_3$-passivated PbS CQD thin films, samples A and B with different dot sizes. The measurements were performed at room temperature using an excitation laser wavelength of 375 nm, and two dominant radiative PL emission peaks located at 1169 and 1553 nm were observed for Sample A. The 1169 nm PL emission peak corresponds to the band-edge excitonic recombination (PbS is a direct bandgap semiconductor) including transitions a and b/c (Figure 3) but is dominated by the free exciton recombination (transition a) at room temperature.[61] The 1553 nm emission peak originates from recombinations that occur through donors/acceptors (transitions e/f, Figure 3) arising from unpassivated surface states, structural defects, or other chemical changes induced during ligand exchange processes. In contrast, only the band-edge excitonic recombination peak (1232 nm) is observed for sample B. When compared with PL spectra of other CQD thin films with different QD sizes (Figure 5(b)), although the CQD and thin-film synthesis processes are the same, it is found that these PL peaks are quantum dot size dependent, indicating a complexity of surface passivation mechanism which requires further investigation.

The surfaces of CQDs typically contain a large amount of recombination centers because of the abrupt termination of the semiconductor crystal periodicity even within a QD. The absence of sub-bandgap-state-related emissions implies better surface passivation of sample B than A, revealing the inevitable diversity of the lab fabrication processes. It is also reasonable that sample A, with a smaller dot size (due to its wider bandgap from PL characterization) that leads to higher surface-to-volume ratio, incorporates more trap states, making itself a more difficult candidate for surface passivation. From Figure 5(a), energy bandgaps of samples A and B were calculated to be ca. 1.1 and 1.0 eV, respectively. The emission from sub-bandgap states in sample A is ca. 0.3 eV lower than the band-edge emissions. In Figure 5(a), sample A has a smaller fwhm (full width at half-maximum) than sample B, reflecting a narrower quantum dot size distribution, as the broadening of PL peaks arises from the quantum dot size polydispersity with specific spectral components originating from dots of specific

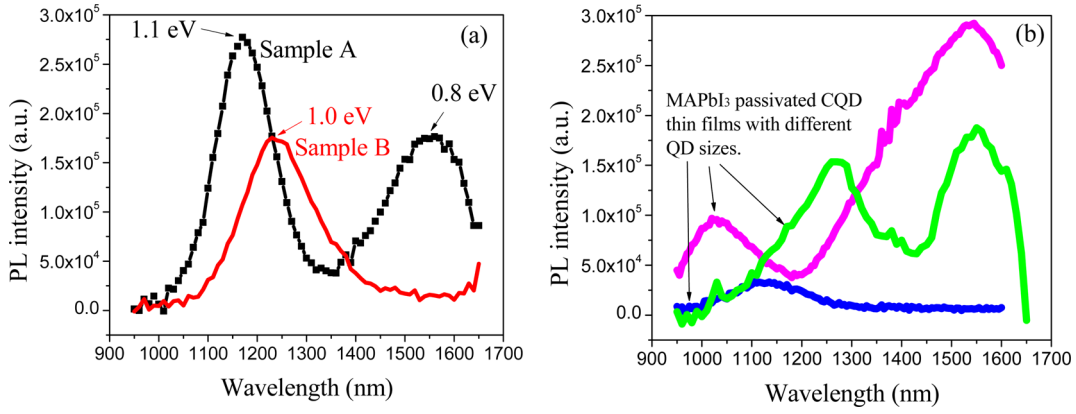

Figure 5. (a) Photoluminescence (PL) spectra of $MAPbI_3$-passivated PbS ($MAPbI_3$–PbS) thin films (samples A and B) spin-coated on glass substrates. (b) PL spectra of $MAPbI_3$–PbS thin films fabricated through the same process as that of samples A and B but with different QD sizes.

DOI: 10.1021/acs.jpcc.6b04468
J. Phys. Chem. C 2016, 120, 14416−14427

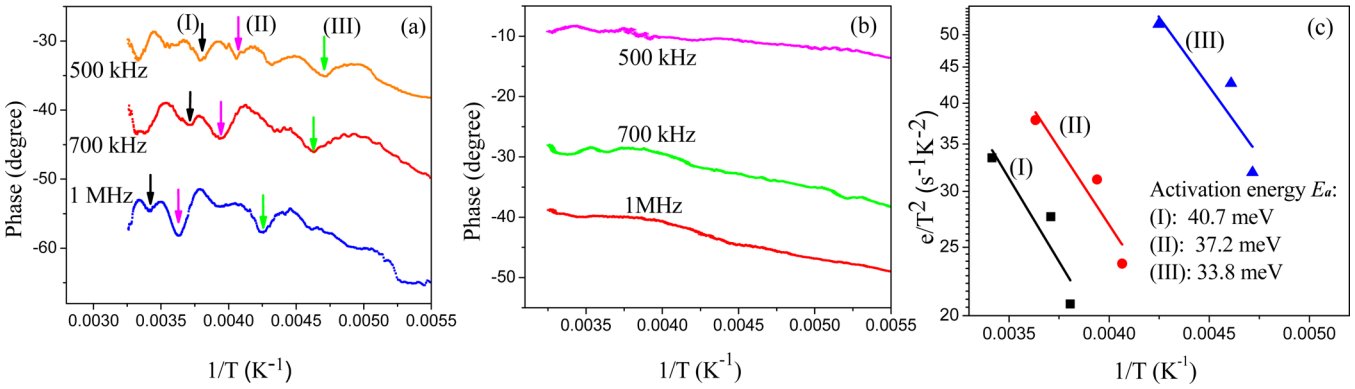

Figure 6. Photocarrier radiometry (PCR) photothermal spectra of $MAPbI_3$-passivated PbS ($MAPbI_3$–PbS) thin films spin-coated on glass substrates, samples A (a) and B (b). (c) Arrhenius plots of the PCR phase troughs, I, II, and III, as shown in (a) and best-fitted to eq 12 for the extraction of activation energies for each sub-bandgap trap level.

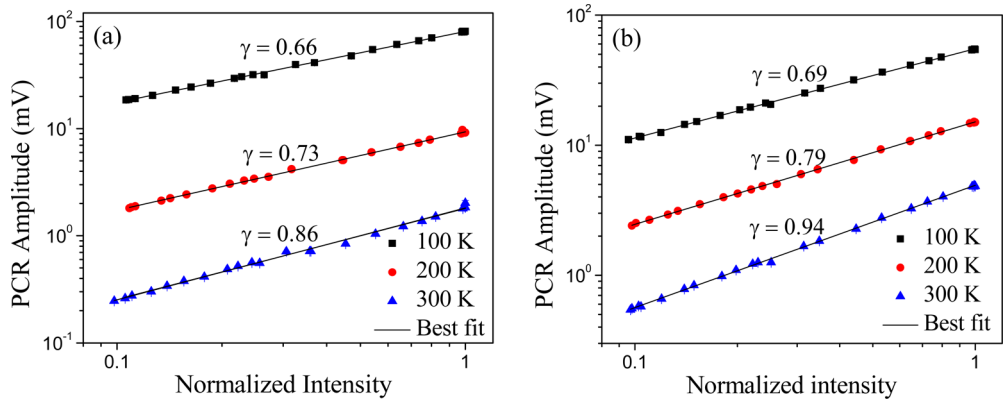

Figure 7. PCR amplitude vs excitation power at three different temperatures for sample A (a) and sample B (b), at 10 kHz laser modulation frequency.

sizes. It should be noted that with the use of a long-pass filter PL emission detected by the InGaAs camera is in a wavelength range from 1000 to 1700 nm.

Further investigation of sub-bandgap states using PCR photothermal spectroscopy is presented in Figure 6. Incorporated within the PCR system, photothermal spectra were obtained through linear temperature scans by measuring PCR signals from the sample at a fixed laser modulation frequency, while the temperature was reduced from 300 to 100 K at a sufficiently slow (quasi-equilibrium) rate of 5 °C/min using the Linkam LTS350 cryogenic stage. From Figures 6(a) and (b), corresponding to samples A and B, respectively, it is seen that sample A exhibits more and deeper troughs at all frequencies. Furthermore, these troughs shift toward higher temperature with increasing modulation frequency of the excitation laser which can be attributed to three dominant sub-bandgap (trap state) levels: (I), (II), and (III). Thermal emission rates of carriers from trap states are temperature-dependent processes. When the emission rate matches (or is resonant with) the modulation frequency (a process called "rate window"), a dynamic photoluminescence (PCR signal) enhancement occurs due to the increased number of free detrapped carriers recombining radiatively, exhibiting a peak in the amplitude of the photothermal spectrum at the resonance temperature. Amplitude peaks and phase troughs follow opposite trends; i.e. ,when there is an amplitude peak in the amplitude spectrum, a trough forms in a corresponding phase spectrum. The phase signal is more sensitive than the amplitude channel which can be influenced easily by, for example, sample surface reflections and shallow surface states. The phase locks on the rate of the photothermal emissions only and is a little or not sensitive to factors complicating the amplitude spectrum. For an optoelectronic sample with one or more traps like the one in Figure 6(a), the phase trough associated with a trap state characterized by a fixed carrier detrapping energy E_a shifts to higher temperatures with increasing modulation frequency. This is caused by the change in the rate-window resonance condition between the faster thermal ejection rate of trapped carriers at the higher temperature (a Boltzmann factor, eq 12) and the modulation frequency, which is now satisfied at a higher frequency.[62,63] The activation energy of sub-bandgap trap levels in sample A can be calculated through Arrhenius-plot fitting of the photothermal emission rate, e_n[62]

$$e_n(T) = R_n \sigma_n \exp\left(-\frac{E_a}{kT}\right) \tag{12}$$

Here R_n is a material constant, and σ_n is the exciton capture cross section. At each trough, $e_n(T_{trough}) = 2.869f$, in which f is the pulse repetition frequency.[63] Figure 6(c) shows the best-fitted activation energies for three dominant sub-bandgap levels in sample A. These sub-bandgap trap levels exhibit similar activation energies ranging from 33.8 to 40.7 meV. Associated with colloidal environment and surface states in PbS QDs, these shallow level multienergetic traps can capture excitons which undergo nonradiative recombinations or phonon-mediated radiative emissions.[48] Activation energies for trap

DOI: 10.1021/acs.jpcc.6b04468
J. Phys. Chem. C 2016, 120, 14416–14427

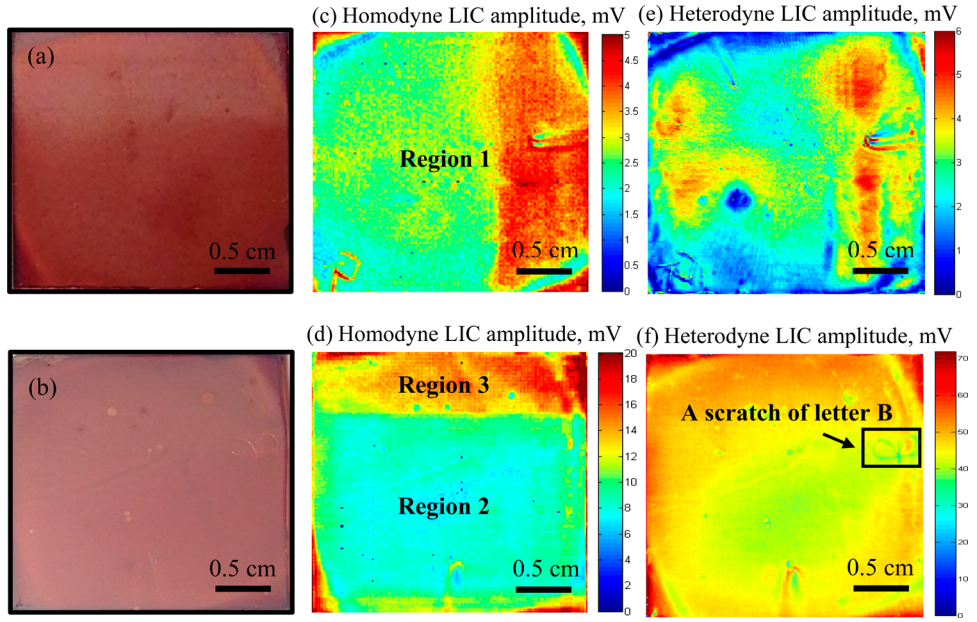

Figure 8. Photos of $MAPbI_3$–PbS thin films, (a) sample A and (b) sample B. 1 kHz homodyne LIC amplitude images of $MAPbI_3$–PbS thin films, (c) sample A and (d) sample B. 20 kHz heterodyne LIC amplitude images of $MAPbI_3$–PbS thin films, (e) sample A and (f) sample B. Note the very different signal strength scales associated with the two samples.

states in EDT-passivated PbS QDs have also been measured by Bozyigit et al.[36] using thermal admittance spectroscopy to be around 100 meV for QDs with an energy bandgap of 1.1 eV. Activation energy differences mostly originate from different exchange ligands. Chuang et al.[54] also reported a ∼230 meV energy difference (activation energy) between band-edge and sub-bandgap state emission using PL, which is close to ∼260 meV following the model proposed by ref 36 for an EDT-treated PbS CQD with an energy bandgap of 1.1 eV. As shown in Figure 2(b), which incorporates information from PL spectroscopy and photothermal temperature scans, there are two trap levels located in the PbS QD bandgap: a deep level (E_a = 0.3 eV) and shallow levels (E_a in a range from 33.8 to 40.7 meV). As shown in Figure 2(b), when excitons are free roaming they may experience radiative recombination, become captured in trap states, or diffuse to the next QD through nearest-neighbor hopping (NNH). The coupling strength between two QDs induces exciton dissociation into free charge carriers. Trapped excitons require overcoming an activation energy barrier to become detrapped and undergo radiative recombinations. For shallow states, the activation energy can be provided by thermal energy; therefore, PCR photothermal spectroscopy with a lock-in rate window can reveal shallow trap states. With regard to sample B, Figure 6(b) shows that the PCR thermal spectra are much smoother at all frequencies, indicative of very few sub-bandgap states in this sample and consistent with the PL spectroscopy results (Figure 5(a)).

To identify charge carrier transition types of various radiative recombination processes for the study of nonlinear PCR responses, Figure 7 shows the excitation power dependent PCR signals of sample A and B at three temperatures (300, 200, and 100 K). Based on the foregoing discussion of radiative recombination processes, experimental data were fitted to $I \propto P^{\gamma}$. At room temperature (300 K), the γ value of sample A was 0.86 which is close to, but less than, unity and is indicative of donor-/acceptor-related free-to-bound exciton recombinations. However, according to the PL spectrum in Figure 5(a), free-exciton-like transitions also exist. By comparison, the only dominant emission peak (i.e., the excitonic recombination) of sample B results in a γ value of 0.94, and the small deviation from unity is probably due to the very few sub-bandgap trap states involved in nonradiative exciton trapping which compromises only slightly the strength of the PCR amplitude, much less so than that of the trap-rich sample A. Both samples exhibited reduced γ values when temperature decreased. The values of γ at 100 K for both samples are close to 0.7 which is likely indicative of the onset of free-to-bound transitions (γ = 0.5) starting to dominate the radiative emission processes as opposed to free-exciton-like emissions (γ = 1). This can be explained by the following typical behavior of exchange-coupled excitons. The presence of bright and dark states can be attributed to the nonstoichiometry of QD surfaces,[64] lattice mismatch during ligand exchange processes, and incomplete surface bond termination or chemical changes.[65] Although the presence of these exciton bright and dark states has not been proven directly, evidence of the presence of these states is accumulating.[66−69] De Lamaestre et al.[66] studied the temperature-dependent PL intensity and decay rates of PbS nanocrystals in a silicate glass and found a large energy splitting (ca. 30 meV) of the exciton ground state fine structure which showed evidence for the existence of a triplet state. Nordin et al.[67] has observed the PL emission from two active states with an energy separation of ca. 6 meV that is close to the theoretically reported energy difference between triplet and singlet states, ca. 10 meV. Gaponenko et al.[68] provided another piece of evidence using steady-state and time-resolved PL and developed a theoretical energy-level model considering the lowest 1S−1S exciton state splitting that can present a consistent quantitative description of experimental results. Gao et al.[69] discussed charge trapping in bright and dark states of coupled PbS quantum dot films with analysis of temperature-dependent PL from dots of different sizes or different surface passivation. Considering the state splitting, although the physics behind the γ exponent decrease with decreasing temperature is

DOI: 10.1021/acs.jpcc.6b04468
J. Phys. Chem. C 2016, 120, 14416−14427

Table 1. Summary of Best-Fitted Parameters using Equation 9

	region 1 (sample a)	region 2 (sample b)	region 3 (sample b)
D_h (cm^2/s)	0.0181 ± 0.0061	0.0106 ± 0.0049	0.00870 ± 0.00437
τ_E (μs)	0.43 ± 0.10	1.56 ± 0.48	2.05 ± 0.20
ΔE (meV)	25.3 ± 3.1	25.4 ± 3.6	25.5 ± 3.2
τ_i (ns)	1.33 ± 0.62	0.75 ± 0.45	2.92 ± 0.78
N_T ($\times 10^{13}$ s^{-1})	20.05 ± 2.30	2.99 ± 0.35	3.18 ± 0.38
β ($\times 10^7$ cm^{-1})	4.55 ± 0.87	1.58 ± 0.49	1.30 ± 0.53
G_o ($\times 10^{25}$ cm^{-2}/s)	4.85 ± 0.69	4.94 ± 0.72	5.03 ± 0.70

not well understood, it is well-known that triplet exciton states with spin 1 (parallel spins) are energetically more stable than singlet exciton states with spin 0 (antiparallel spins). Furthermore, triplet states have a higher statistical weight of 3 (allowed values of spin components: −1, 0, and 1) than that of singlet states (statistical weight = 1, spin component 0). Consequently, at low temperatures, most excitons condense into triplet states, from which they cannot decay radiatively to the S = 0 ground state. However, triplet excitons have longer lifetimes and higher probability for nonradiative recombination than deeper dark states. As a result, the contribution of excitonic recombinations to dynamic PL (measured by PCR) decreases with reduced temperature in favor of nonradiative triplet recombinations. It is concluded that the presence of large densities of trap states can reverse the nonradiative recombination suppression rate at low temperatures previously observed due to decreased phonon populations in PbS CQD thin films.[48] Instead, enhanced nonradiative recombinations reduce the radiative emission, an effect which may severely compromise the solar efficiency of photovoltaic solar cells fabricated using this type of CQDs.

Figure 8(a) and (b) presents photos of $MAPbI_3$-passivated PbS thin films. The thin films were spin-coated on glass substrates with an area of 25 × 25 mm^2 and stored together in nitrogen environment for further study. It is observed that these thin films are visually homogeneous with few visible imperfections. From a series of CQD thin films with different QD size, we have experimentally observed that the CQD thin-film color changes slightly with QD size. This is consistent with the expected change in quantum confinement which affects the optical absorption coefficient of these quantum dots, thereby accounting for the slight color difference between Figure 8(a) and (b). In contrast, homodyne and heterodyne LIC images shown in Figure 8(c)−(f) illustrates significant degrees of inhomogeneity. The physical origins of the LIC spatial contrast are due to the free photocarrier density diffusion-wave distributions, which depend on charge carrier transport parameters, mainly the effective exciton lifetime as well as the hopping diffusivity, detrapping time, and trap state density as shown in eq 9. Specifically, large amplitudes and phase lags correspond to high photocarrier density, a result of long local carrier lifetimes; however, for regions associated with mechanical damages or intrinsic material defects, lower amplitude is generally expected because defects lead to a significant increase of nonradiative recombination rates resulting in a reduction of carrier lifetimes. Comparison between regions 2 and 3 in Figure 8(d) provides a direct example of the LIC image contrast arising from different photocarrier diffusion-wave distributions, with region 3 being indicative of longer carrier lifetimes. This may be due to different spin-coating and ligand passivation processes or unexpected surface chemical reactions upon exposure to ambient air. Regarding mechanical-damage-induced defects as shown in Figure 8(f), the area of a scratched letter B on the front surface of sample B exhibits lower PCR amplitude values compared with its neighboring regions. This is attributed to the damage-induced lower photocarrier density diffusion wave, leading to enhanced probability of nonradiative recombinations into defect states, thus shorter lifetimes. It should be noted that the scratch was produced after the homodyne image of sample B was obtained and shown in Figure 8(d). For both A and B, homodyne and heterodyne LIC amplitude images show prominent inhomogeneities in the charge carrier density distributions.

The spatial resolution of LIC images is determined by the ac hopping diffusion length through

$$L(\omega) = \sqrt{\frac{D_h \tau_E}{1 + i\omega\tau_E}} \tag{13}$$

Shorter $L(\omega)$ yields higher spatial resolution that can be achieved through increasing the angular modulation frequency ω. Limited by the camera frame rate and exposure time, the highest frequency achieved in this study with homodyne lock-in carrierography is 1 kHz for high-quality images. However, better image resolution relies on higher laser modulation frequencies,[42−46] so heterodyne imaging was performed at 20 kHz. Higher frequency imaging is limited by the low radiative emissions of our samples but can be attained by using laser sources with higher power. Compared with Figure 8(c), Figure 8 (e) exhibits higher spatial resolution with more detailed features of charge carrier density wave distributions. As for sample B, Figure 8(f) with a laser frequency of 20 kHz exhibits limited image resolution improvement when compared with Figure 8(d). This is probably due to the longer effective exciton lifetimes of sample B than A, as shown in Table 1 through PCR frequency characterization and computational best fits, leading to a much smaller change of the longer hopping diffusion length $L(\omega)$, eq 13.

To investigate exciton transport parameters and material properties of $MAPbI_3$-passivated PbS CQD thin films, PCR frequency scans and theoretical best-fits were performed. Sample surface spots were selected as shown in Figure 8(c), (d) from regions 1 to 3. Equation 9 was used to fit the experimental PCR data for the extraction of parameters involved. It is important to note that the PCR phase channel is calculated through $\varphi(\omega) = \tan^{-1}\left[\frac{F_I(\omega)}{F_R(\omega)}\right]$, where $F_I(\omega)$ and $F_R(\omega)$ are, respectively, the imaginary and real parts of eq 9. Figure 9 presents the PCR frequency scans of the three regions as well as the best-fits of eq 9 to each curve. Region 1 exhibits a smaller phase lag than regions 2 and 3, indicating shorter lifetime,[57,48] while region 3 exhibits slightly larger phase lag

DOI: 10.1021/acs.jpcc.6b04468
J. Phys. Chem. C 2016, 120, 14416−14427

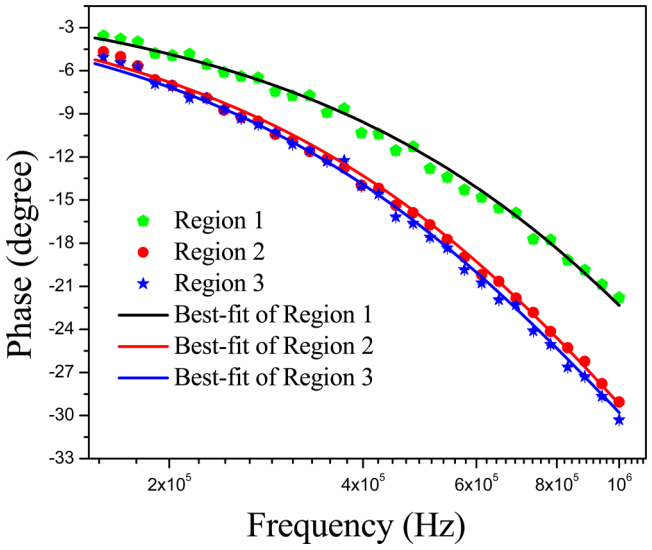

Figure 9. Phase diagram of PCR frequency scans in three different regions 1−3 as shown in Figure 8(c),(d) and the best-fits of experimental data to eq 9.

than region 2, consistent with the slightly longer lifetime of region 3.

The best fitting program was implemented through an fminsearch solver minimizing the square sum of errors between the experimental and calculated data. To establish the uniqueness and reliability of our measurements, different starting points were generated automatically by the solver for each fitting process, so that the best-fitted results fluctuated about their mean values. The fitting procedure was repeated several hundred times, and 100 sets of results with the smallest variance were selected for statistical calculation as tabulated in Table 1. The table summarizes the best-fitted carrier transport and material property parameters including D_h, τ_E, ΔE, τ_i, N_T, β, and G_o for the three regions, providing room-temperature measurements. The CQD thickness of 200 nm was measured by scanning electron microscopy. Region 3 exhibits the highest effective exciton lifetime of 2.05 ± 0.20 μs, consistent with the LIC image results. The relatively long lifetime could be the effect of dielectric screening similar to that observed in other IV−VI semiconductor nanocrystals.[70] Similar theoretical results of exciton lifetimes have also been reported to be in a range between 1 and 3 μs for PbS CQDs and PbSe CQDs.[71] Additional same range experimental data have been reported in the literature from time-resolved PL spectroscopy: between 4.97 and 2.74 μs for small PbSe CQDs with diameter from 2.7 to 4.7 nm;[72] 1 μs for oleic-acid-capped PbS CQDs;[70] and 2.5−0.9 μs for PbSe CQDs, 3.2−4.3 nm in diameter.[73] Furthermore, both our A and B samples exhibit D_h values on the order of 10^{-2} cm^2/s. Comparable results using transient PL spectroscopy for 3-mercaptopropionic acid (MPA) ligands or 8-mercaptooctanoic acid (MOA) linked PbS CQDs were also reported elsewhere.[74] Those PbS QDs were doped with metal nanoparticles to introduce fixed exciton dissociation distances away from the location of their formation. The best-fitted separation energy ΔE between singlet and triplet states is ca. 25 meV, which indirectly provides another piece of evidence for the existence of dark and bright states in PbS CQDs. Manifestations of the existence of these states in PbS CQD thin films with similar separation energies were also reported elsewhere.[48] Consistent with the PL spectra in Figure 5(a), Table 1 exhibits that region 1 has the highest carrier trapping rate N_T, indicating the highest trap state density among all three regions. Table 1 further presents the detrapping lifetimes, τ_i, reflecting the time an exciton resides in a trap state before being released. The detrapping activation energies obtained from Figure 6(c) are tentatively attributed to phonon-mediated photothermal interactions, and the associated interface trap states appear in the energy diagram of Figure 2(b). Room-temperature NNH and the carrier diffusivity D_h are determined by the interdot coupling strength. The absorption coefficient β was evaluated through best-fitting to be on the order of 10^7 cm^{-1} for the 800 nm excitation. For comparison, an absorption coefficient on the order of 10^5 cm^{-1} for excited oleic acid-capped PbS CQDs suspended in tetrachloroethylene (C_2Cl_4)[71] was measured using a UV−vis−NIR spectrophotometer. Furthermore, using the same method, the PbSe CQD bandgap absorption coefficient was found to be ∼10^6 cm^{-1} and decreased with the dot size.[75] It is hypothesized that these large differences may arise from different surface passivation ligands, dot dimensions, and sample state (solvent/solid). Finally, the exciton generation rate G_o is an excitation source determined parameter which essentially remains constant across the three regions 1−3, as expected.

Apart from fitting uniqueness, sample stability is also essential for measurement accuracy; hence, sample stability was examined under laser excitation for the duration of one complete PCR frequency scan. Figure 10 illustrates the sample

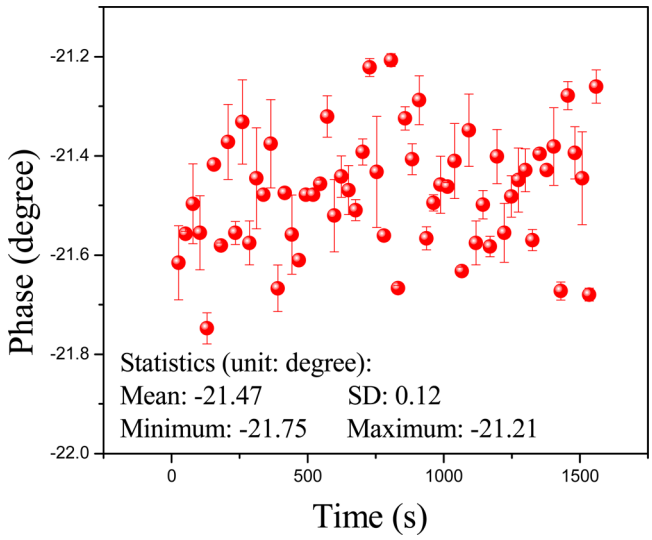

Figure 10. PCR phase dependence on time over 25 min, the duration of a PCR frequency scan. Sample A at 100 kHz laser modulation frequency.

A PCR phase time dependence measured at 100 kHz over 25 min. It exhibits a standard deviation of only 0.12°, which allows us to conclude that the PCR phase is not time dependent and the excitation laser has negligible influence on CQD thin films.

Coupled with the theoretical best-fits, a conclusion can be reached that in Figure 2(b) excitons undergo recombinations or dissociate into free charge carriers which can recombine radiatively through donors/acceptors or through trap-state-induced nonradiative transitions, giving rise to nonlinear heterodyne LIC image responses to laser excitation. The combined PCR, LIC imaging, and photothermal temperature scans of perovskite-shelled PbS CQD thin films were shown to

DOI: 10.1021/acs.jpcc.6b04468
J. Phys. Chem. C 2016, 120, 14416−14427

yield quantitative information about key exciton transport processes like effective lifetimes and other hopping transport parameters extracted from the theoretical exciton diffusion-wave density trap model, eq 9.

5. CONCLUSIONS

High frequency InGaAs-camera-based homodyne and heterodyne LIC images of CQD thin films, as well as temperature-scanned photothermal emission rates, activation energies, and trap densities were obtained for the first time to qualitatively characterize CQD nanolayer properties. It was demonstrated that a $MAPbI_3$-shelled PbS CQD thin film exhibits nonlinear PCR signal response that acts as an effective frequency mixer giving rise to heterodyne LIC images, originating from free-to-bound and trap-state-associated recombination. Furthermore, quantitative analysis of exciton transport processes using PCR frequency scans became possible using theoretical best-fits to PCR exciton hopping theory that yielded carrier transport parameters including effective exciton lifetimes and diffusivities of $MAPbI_3$-passivated CQD. The quantitative analysis provided support to the hypothesis of the existence of bright and dark states in PbS CQDs and was used to extract several transport parameters of our perovskite-shelled PbS CQD thin films. Combined with LIC imaging, PCR frequency scans and photothermal temperature scans can provide fast, quantitative, contactless, nondestructive evaluation of charge carrier transport as well as material properties of CQD materials and electronic devices. This combined analytical methodology can be used for improved control of PbS CQD solar cell fabrication and performance/efficiency optimization.

AUTHOR INFORMATION

Corresponding Author

*E-mail: mandelis@mie.utoronto.ca. Phone: (416) 978 5106. Fax: (416) 978 7753.

Notes

The authors declare no competing financial interest.

ACKNOWLEDGMENTS

The authors are grateful to the Natural Sciences and Engineering Research Council of Canada (NSERC) for a Discovery grant to AM, and the Canada Research Chairs program.

REFERENCES

(1) Graetzel, M.; Janssen, R. A.; Mitzi, D. B.; Sargent, E. H. Materials interface engineering for solution-processed photovoltaics. *Nature* **2012**, *488*, 304−312.
(2) Gong, X.; Yang, Z.; Walters, G.; Comin, R.; Ning, Z.; Beauregard, E.; Adinolfi, V.; Voznyy, O.; Sargent, E. H. Highly efficient quantum dot near-infrared light-emitting diodes. *Nat. Photonics* **2016**, *10*, 253−257.
(3) Hillhouse, H. W.; Beard, M. C. Solar cells from colloidal nanocrystals: Fundamentals, materials, devices, and economics. *Curr. Opin. Colloid Interface Sci.* **2009**, *14*, 245−259.
(4) Kramer, I. J.; Sargent, E. H. Colloidal quantum dot photovoltaics: A path forward. *ACS Nano* **2011**, *5*, 8506−8514.
(5) Ning, Z.; Gong, X.; Comin, R.; Walters, G.; Fan, F.; Voznyy, O.; Yassitepe, E.; Buin, A.; Hoogland, S.; Sargent, E. H. Quantum-dot-in-perovskite solids. *Nature* **2015**, *523*, 324−328.
(6) Sargent, E. H. Infrared quantum dots. *Adv. Mater.* **2005**, *17*, 515−522.
(7) Tang, J.; Sargent, E. H. Infrared colloidal quantum dots for photovoltaics: Fundamentals and recent progress. *Adv. Mater.* **2011**, *23*, 12−29.
(8) Sargent, E. H. Colloidal quantum dot solar cells. *Nat. Photonics* **2012**, *6*, 133−135.
(9) Konstantatos, G.; Sargent, E. H. *Colloidal quantum dot optoelectronics and photovoltaics*; Sargent, E. H., Eds.; Cambridge University Press: Cambridge, U.K., 2013.
(10) Pattantyus-Abraham, A. G.; Kramer, I. J.; Barkhouse, A. R.; Wang, X.; Konstantatos, G.; Debnath, R.; Levina, L.; Raabe, I.; Nazeeruddin, M. K.; Gratzel, M.; et al. Depleted-heterojunction colloidal quantum dot solar cells. *ACS Nano* **2010**, *4*, 3374−3380.
(11) Lan, X.; Voznyy, O.; Kiani, A.; García de Arquer, F. P.; Abbas, A. S.; Kim, G. H.; Liu, M.; Yang, Z.; Walters, G.; Xu, J.; et al. Passivation using molecular halides increases quantum dot solar cell performance. *Adv. Mater.* **2016**, *28*, 299−304.
(12) Yang, Z.; Janmohamed, A.; Lan, X.; García de Arquer, F. P.; Voznyy, O.; Yassitepe, E.; Kim, G. H.; Ning, Z.; Gong, X.; Comin, R.; et al. Colloidal quantum dot photovoltaics enhanced by perovskite shelling. *Nano Lett.* **2015**, *15*, 7539−7543.
(13) Chuang, C. H. M.; Brown, P. R.; Bulović, V.; Bawendi, M. G. Improved performance and stability in quantum dot solar cells through band alignment engineering. *Nat. Mater.* **2014**, *13*, 796−801.
(14) Liu, M.; de Arquer, F.; Li, Y.; Lan, X.; Kim, G. H.; Voznyy, O.; Jagadamma, L. K.; Abbas, A. S.; Hoogland, S.; Lu, Z.; et al. Double-Sided Junctions Enable High-Performance Colloidal-Quantum-Dot Photovoltaics. *Adv. Mater.* **2016**, *28*, 4142−4148.
(15) http://www.nrel.gov/ncpv/images/efficiency_chart.jpg (accessed June 22, 2016).
(16) Huynh, W. U.; Dittmer, J. J.; Alivisatos, A. P. Hybrid nanorod-polymer solar cells. *Science* **2002**, *295*, 2425−2427.
(17) Konstantatos, G.; Howard, I.; Fischer, A.; Hoogland, S.; Clifford, J.; Klem, E.; Levina, L.; Sargent, E. H. Ultrasensitive solution-cast quantum dot photodetectors. *Nature* **2006**, *442*, 180−183.
(18) Kovalenko, M. V.; Scheele, M.; Talapin, D. V. Colloidal nanocrystals with molecular metal chalcogenide surface ligands. *Science* **2009**, *324*, 1417−1420.
(19) Ning, Z.; Ren, Y.; Hoogland, S.; Voznyy, O.; Levina, L.; Stadler, P.; Lan, X.; Zhitomirsky, D.; Sargent, E. H. All-inorganic colloidal quantum dot photovoltaics employing solution-phase halide passivation. *Adv. Mater.* **2012**, *24*, 6295−6299.
(20) Jang, J.; Liu, W.; Son, J. S.; Talapin, D. V. Temperature-dependent hall and field-effect mobility in strongly coupled all-inorganic nanocrystal arrays. *Nano Lett.* **2014**, *14*, 653−662.
(21) Dirin, D. N.; Dreyfuss, S.; Bodnarchuk, M. I.; Nedelcu, G.; Papagiorgis, P.; Itskos, G.; Kovalenko, M. V. Lead halide perovskites and other metal halide complexes as inorganic capping ligands for colloidal nanocrystals. *J. Am. Chem. Soc.* **2014**, *136*, 6550−6553.
(22) Zhang, H.; Jang, J.; Liu, W.; Talapin, D. V. Colloidal nanocrystals with inorganic halide, pseudohalide, and halometallate ligands. *ACS Nano* **2014**, *8*, 7359−7369.
(23) Ning, Z.; Voznyy, O.; Pan, J.; Hoogland, S.; Adinolfi, V.; Xu, J.; Li, M.; Kirmani, A. R.; Sun, J. P.; Minor, J.; et al. Air-stable n-type colloidal quantum dot solids. *Nat. Mater.* **2014**, *13*, 822−828.
(24) Cassagneau, T.; Mallouk, T. E.; Fendler, J. H. Layer-by-layer assembly of thin film zener diodes from conducting polymers and CdSe nanoparticles. *J. Am. Chem. Soc.* **1998**, *120*, 7848−7859.
(25) Shimomura, M.; Sawadaishi, T. Bottom-up strategy of materials fabrication: A new trend in nanotechnology of soft materials. *Curr. Opin. Colloid Interface Sci.* **2001**, *6*, 11−16.
(26) Fu, Y.; Xu, H.; Bai, S.; Qiu, D.; Sun, J.; Wang, Z.; Zhang, X. Fabrication of a stable polyelectrolyte/Au nanoparticles multilayer film. *Macromol. Rapid Commun.* **2002**, *23*, 256−259.
(27) Guo, Q.; Kim, S. J.; Kar, M.; Shafarman, W. N.; Birkmire, R. W.; Stach, E. A.; Agrawal, R.; Hillhouse, H. W. Development of $CuInSe_2$ nanocrystal and nanoring inks for low-cost solar cells. *Nano Lett.* **2008**, *8*, 2982−2987.
(28) Wood, V.; Panzer, M. J.; Chen, J.; Bradley, M. S.; Halpert, J. E.; Bawendi, M. G.; Bulović, V. Inkjet-printed quantum dot−polymer

DOI: 10.1021/acs.jpcc.6b04468
J. Phys. Chem. C 2016, 120, 14416−14427

composites for full-color AC-driven displays. *Adv. Mater.* **2009**, *21*, 2151−2155.
(29) Yang, C. C.; Josefowicz, J. Y.; Alexandru, L. Deposition of ultrathin films by a withdrawal method. *Thin Solid Films* **1980**, *74*, 117−127.
(30) Labelle, A. J.; Thon, S. M.; Masala, S.; Adachi, M. M.; Dong, H.; Farahani, M.; Ip, A. H.; Fratalocchi, A.; Sargent, E. H. Colloidal quantum dot solar cells exploiting hierarchical structuring. *Nano Lett.* **2015**, *15*, 1101−1108.
(31) Labelle, A. J.; Thon, S. M.; Kim, J. Y.; Lan, X.; Zhitomirsky, D.; Kemp, K. W.; Sargent, E. H. Conformal fabrication of colloidal quantum dot solids for optically enhanced photovoltaics. *ACS Nano* **2015**, *9*, 5447−5453.
(32) Kramer, I. J.; Minor, J. C.; Moreno-Bautista, G.; Rollny, L.; Kanjanaboos, P.; Kopilovic, D.; Thon, S. M.; Carey, G. H.; Chou, K. W.; Zhitomirsky, D.; et al. Efficient spray-coated colloidal quantum dot solar cells. *Adv. Mater.* **2015**, *27*, 116−121.
(33) Kramer, I. J.; Moreno-Bautista, G.; Minor, J. C.; Kopilovic, D.; Sargent, E. H. Colloidal quantum dot solar cells on curved and flexible substrates. *Appl. Phys. Lett.* **2014**, *105*, 163902.
(34) Yang, Z.; Janmohamed, A.; Lan, X.; García de Arquer, F. P.; Voznyy, O.; Yassitepe, E.; Kim, G. H.; Ning, Z.; Gong, X.; Comin, R.; et al. Colloidal quantum dot photovoltaics enhanced by perovskite shelling. *Nano Lett.* **2015**, *15*, 7539−7543.
(35) Sun, Z.; Sitbon, G.; Pons, T.; Bakulin, A. A.; Chen, Z. Reduced carrier recombination in PbS-CuInS2 quantum dot solar cells. *Sci. Rep.* **2015**, *5*, 10626.
(36) Bozyigit, D.; Lin, W. M.; Yazdani, N.; Yarema, O.; Wood, V. A quantitative model for charge carrier transport, trapping and recombination in nanocrystal-based solar cells. *Nat. Commun.* **2015**, *6*, 6180.
(37) Colbert, A. E.; Wu, W.; Janke, E. M.; Ma, F.; Ginger, D. S. Effects of ligands on charge generation and recombination in hybrid polymer/quantum dot solar cells. *J. Phys. Chem. C* **2015**, *119*, 24733−24739.
(38) Melnikov, A.; Mandelis, A.; Tolev, J.; Chen, P.; Huq, S. Infrared lock-in carrierography (photocarrier radiometric imaging) of Si solar cells. *J. Appl. Phys.* **2010**, *107*, 114513.
(39) Tran, T. M. H.; Pieters, B. E.; Schneemann, M.; Müller, T. C. M.; Gerber, A.; Kirchartz, T.; Rau, U. Quantitative evaluation method for electroluminescence images of a-Si: H thin-film solar modules. *Phys. Status Solidi RRL* **2013**, *7*, 627−630.
(40) Mandelis, A.; Melnikov, A. Method and apparatus for performing heterodyne lock-in imaging and quantitative non-contact measurements of electrical properties. U.S. Patent 9,131,170, September 8, 2015.
(41) Mandelis, A.; Zhang, Y.; Melnikov, A. Statistical theory and applications of lock-in carrierographic image pixel brightness dependence on multi-crystalline Si solar cell efficiency and photovoltage. *J. Appl. Phys.* **2012**, *112*, 054505.
(42) Sun, Q. M.; Melnikov, A.; Mandelis, A. Camera-based lock-in and heterodyne carrierographic photoluminescence imaging of crystalline silicon wafers. *Int. J. Thermophys.* **2015**, *36*, 1274−1280.
(43) Sun, Q.; Melnikov, A.; Mandelis, A. Camera-based high frequency heterodyne lock-in carrierographic (frequency-domain photoluminescence) imaging of crystalline silicon wafers. *Phys. Status Solidi A* **2016**, *213*, 405−411.
(44) Sun, Q.; Melnikov, A.; Mandelis, A. Quantitative self-calibrating lock-in carrierographic lifetime imaging of silicon wafers. *Appl. Phys. Lett.* **2012**, *101*, 242107.
(45) Melnikov, A.; Mandelis, A.; Tolev, J.; Chen, P.; Huq, S. Infrared lock-in carrierography (photocarrier radiometric imaging) of Si solar cells. *J. Appl. Phys.* **2010**, *107*, 114513.
(46) Melnikov, A.; Chen, P.; Zhang, Y.; Mandelis, A. Lock-in and heterodyne carrierographic imaging characterization of industrial multicrystalline silicon solar cells. *Int. J. Thermophys.* **2012**, *33*, 2095−2102.
(47) Mandelis, A.; Batista, J.; Shaughnessy, D. Infrared photocarrier radiometry of semiconductors: Physical principles, quantitative depth profilometry, and scanning imaging of deep subsurface electronic defects. *Phys. Rev. B: Condens. Matter Mater. Phys.* **2003**, *67*, 205208.
(48) Wang, J.; Mandelis, A.; Melnikov, A.; Hoogland, S.; Sargent, E. H. Exciton lifetime broadening and distribution profiles of PbS colloidal quantum dot thin films using frequency-and temperature-scanned photocarrier radiometry. *J. Phys. Chem. C* **2013**, *117*, 23333−23348.
(49) Fonoberov, V. A.; Alim, K. A.; Balandin, A. A.; Xiu, F.; Liu, J. Photoluminescence investigation of the carrier recombination processes in ZnO quantum dots and nanocrystals. *Phys. Rev. B: Condens. Matter Mater. Phys.* **2006**, *73*, 165317.
(50) Tongay, S.; Suh, J.; Ataca, C.; Fan, W.; Luce, A.; Kang, J. S.; Liu, J.; Ko, C.; Raghunathanan, R.; Zhou, J.; et al. Defects activated photoluminescence in two-dimensional semiconductors: Interplay between bound, charged, and free excitons. *Sci. Rep.* **2013**, *3*, 2657.
(51) Saxena, A.; Yang, S.; Philipose, U.; Ruda, H. E. Excitonic and pair-related photoluminescence in ZnSe nanowires. *J. Appl. Phys.* **2008**, *103*, 053109.
(52) Wang, H.; Ji, Z.; Xiao, H.; Wang, M.; Qu, S.; Shen, Y.; Xu, X. Influence of injection current and temperature on electroluminescence in InGaN/GaN multiple quantum wells. *Phys. E* **2014**, *59*, 56−59.
(53) Kim, Y.; Ban, K. Y.; Kuciauskas, D.; Dippo, P. C.; Honsberg, C. B. Impact of delta-doping position on photoluminescence in type-II InAs/GaAsSb quantum dots. *Semicond. Sci. Technol.* **2015**, *30*, 035006.
(54) Chuang, C. H. M.; Maurano, A.; Brandt, R. E.; Hwang, G. W.; Jean, J.; Buonassisi, T.; Bulović, V.; Bawendi, M. G. Open-circuit voltage deficit, radiative sub-bandgap states, and prospects in quantum dot solar cells. *Nano Lett.* **2015**, *15*, 3286−3294.
(55) Moroz, P.; Kholmicheva, N.; Razgoniaeva, N.; Burchfield, D.; Sharma, N.; Acharya, A.; Zamkov, M. Optical techniques for probing the excited state dynamics of quantum dot solids. *Chem. Phys.* **2016**, *471*, 59−68.
(56) Schmidt, T.; Lischka, K.; Zulehner, W. Excitation-power dependence of the near-band-edge photoluminescence of semiconductors. *Phys. Rev. B: Condens. Matter Mater. Phys.* **1992**, *45*, 8989.
(57) Hu, L.; Mandelis, A.; Melnikov, A.; Lan, X.; Hoogland, S.; Sargent, H. E. Exciton hopping transport in PbS colloidal quantum dot thin films using frequency-and temperature-scanned photocarrier radiometry. *Int. J. Thermophys.* **2015**, submitted for publication.
(58) Turyanska, L.; Patane, A.; Henini, M.; Hennequin, B.; Thomas, N. R. Temperature dependence of the photoluminescence emission from thiol-capped PbS quantum dots. *Appl. Phys. Lett.* **2007**, *90*, 101913.
(59) Gaponenko, M. S.; Lutich, A. A.; Tolstik, N. A.; Onushchenko, A. A.; Malyarevich, A. M.; Petrov, E. P.; Yumashev, K. V. Temperature-dependent photoluminescence of PbS quantum dots in glass: Evidence of exciton state splitting and carrier trapping. *Phys. Rev. B: Condens. Matter Mater. Phys.* **2010**, *82*, 125320.
(60) Kostić, R.; Romčević, M.; Romčević, N.; Klopotowski, L.; Kossut, J.; Kuljanin-Jakovljević, J.; Čomor, M. I.; Nedeljković, J. M. Photoluminescence and far-infrared spectroscopy of PbS quantum dots−Polyvinyl alcohol nanocomposite. *Opt. Mater.* **2008**, *30*, 1177−1182.
(61) Bagnall, D. M.; Chen, Y. F.; Shen, M. Y.; Zhu, Z.; Goto, T.; Yao, T. Room temperature excitonic stimulated emission from zinc oxide epilayers grown by plasma-assisted MBE. *J. Cryst. Growth* **1998**, *184*, 605−609.
(62) Xia, J.; Mandelis, A. Broadening effects and ergodicity in deep level photothermal spectroscopy of defect states in semi-insulating GaAs: A combined temperature-, pulse-rate-, and time-domain study of defect state kinetics. *J. Appl. Phys.* **2009**, *105*, 103712.
(63) Xia, J.; Mandelis, A. Noncontact deep level photo-thermal spectroscopy: Technique and application to semi-insulating GaAs wafers. *Appl. Phys. Lett.* **2007**, *90*, 062119.
(64) Hughes, B. K.; Ruddy, D. A.; Blackburn, J. L.; Smith, D. K.; Bergren, M. R.; Nozik, A. J.; Johnson, J. C.; Beard, M. C. Control of PbSe quantum dot surface chemistry and photophysics using an alkylselenide ligand. *ACS Nano* **2012**, *6*, 5498−5506.

DOI: 10.1021/acs.jpcc.6b04468
J. Phys. Chem. C 2016, 120, 14416−14427

(65) Chappell, H. E.; Hughes, B. K.; Beard, M. C.; Nozik, A. J.; Johnson, J. C. Emission quenching in PbSe quantum dot arrays by short-term air exposure. *J. Phys. Chem. Lett.* **2011**, *2*, 889−893.
(66) De Lamaëstre, R. E.; Bernas, H.; Pacifici, D.; Franzo, G.; Priolo, F. Evidence for a″ dark exciton″ state of PbS nanocrystals in a silicate glass. *Appl. Phys. Lett.* **2006**, *88*, 181115.
(67) Nordin, M. N.; Li, J.; Clowes, S. K.; Curry, R. J. Temperature dependent optical properties of PbS nanocrystals. *Nanotechnology* **2012**, *23*, 275701.
(68) Gaponenko, M. S.; Lutich, A. A.; Tolstik, N. A.; Onushchenko, A. A.; Malyarevich, A. M.; Petrov, E. P.; Yumashev, K. V. Temperature-dependent photoluminescence of PbS quantum dots in glass: Evidence of exciton state splitting and carrier trapping. *Phys. Rev. B: Condens. Matter Mater. Phys.* **2010**, *82*, 125320.
(69) Gao, J.; Johnson, J. C. Charge trapping in bright and dark states of coupled PbS quantum dot films. *ACS Nano* **2012**, *6*, 3292−3303.
(70) Warner, J. H.; Thomsen, E.; Watt, A. R.; Heckenberg, N. R.; Rubinsztein-Dunlop, H. Time-resolved photoluminescence spectroscopy of ligand-capped PbS nanocrystals. *Nanotechnology* **2005**, *16*, 175.
(71) Moreels, I.; Lambert, K.; Smeets, D.; De Muynck, D.; Nollet, T.; Martins, J. C.; Vanhaecke, F.; Vantomme, A.; Delerue, C.; Allan, G.; et al. Size-dependent optical properties of colloidal PbS quantum dots. *ACS Nano* **2009**, *3*, 3023−3030.
(72) Kigel, A.; Brumer, M.; Maikov, G.; Sashchiuk, A.; Lifshitz, E. The ground-state exciton lifetime of PbSe nanocrystal quantum dots. *Superlattices Microstruct.* **2009**, *46*, 272−276.
(73) Oron, D.; Aharoni, A.; de Mello Donega, C.; van Rijssel, J.; Meijerink, A.; Banin, U. Universal role of discrete acoustic phonons in the low-temperature optical emission of colloidal quantum dots. *Phys. Rev. Lett.* **2009**, *102*, 177402.
(74) Kholmicheva, N.; Moroz, P.; Bastola, E.; Razgoniaeva, N.; Bocanegra, J.; Shaughnessy, M.; Porach, Z.; Khon, D.; Zamkov, M. Mapping the Exciton Diffusion in Semiconductor Nanocrystal Solids. *ACS Nano* **2015**, *9*, 2926−2937.
(75) Moreels, I.; Lambert, K.; De Muynck, D.; Vanhaecke, F.; Poelman, D.; Martins, J. C.; Allan, G.; Hens, Z. Composition and size-dependent extinction coefficient of colloidal PbSe quantum dots. *Chem. Mater.* **2007**, *19*, 6101−6106.

DOI: 10.1021/acs.jpcc.6b04468
J. Phys. Chem. C 2016, 120, 14416−14427